Published in final edited form as:
*Comput Med Imaging Graph*. 2010 April ; 34(3): 236–249. doi:10.1016/j.compmedimag.2009.10.002.

# THREE-DIMENSIONAL COUPLED-OBJECT SEGMENTATION USING SYMMETRY AND TISSUE TYPE INFORMATION

**Payam Bahmanbijari**[1,2], **Alireza Akhondi-Asl**[1,2], and **Hamid Soltanian-Zadeh**[1,2,3]

Payam Bahmanbijari: p.bijari@ece.ut.ac.ir; Alireza Akhondi-Asl: a.akhundi@ece.ut.ac.ir; Hamid Soltanian-Zadeh: hszadeh@ut.ac.ir

[1] Control and Intelligent Processing Center of Excellence, Electrical and Computer Engineering Department, University of Tehran, Tehran, Iran

[2] School of Cognitive Sciences, Institute for Studies in Theoretical Physics and Mathematics (IPM), Tehran, Iran

[3] Image Analysis Laboratory, Radiology Department, Henry Ford Hospital, Detroit, Michigan, USA

## Abstract

This paper presents an automatic method for segmentation of brain structures using their symmetry and tissue type information. The proposed method generates segmented structures that have homogenous tissues. It benefits from general symmetry of the brain structures in the two hemispheres. It also benefits from the tissue regions generated by fuzzy c-means clustering. All in all, the proposed method can be described as a dynamic knowledge-based method that eliminates the need for statistical shape models of the structures while generating accurate segmentation results. The proposed approach is implemented in MATLAB and tested on the Internet Brain Segmentation Repository (IBSR) datasets. To this end, it is applied to the segmentation of caudate and ventricles three-dimensionally in magnetic resonance images (MRI) of the brain. Impacts of each of the steps of the proposed approach are demonstrated through experiments. It is shown that the proposed method generates accurate segmentation results that are insensitive to initialization and parameter selection. The proposed method is compared to four previous methods illustrating advantages and limitations of each method.

### Keywords

Segmentation; Brain Structures; Symmetry; Fuzzy c-means; Tissue Type Force; Level Set; Deformable Models; Magnetic Resonance Imaging (MRI)

## I. Introduction

Segmentation is the first step in many image analysis and interpretation applications and one of the growing fields of image processing. Segmentation of anatomical structures and extraction of their pathological features from magnetic resonance images (MRI) are challenging problems that are essential for the quantitative evaluation of tissues, structures, and organs of the human body. To this end, a variety of automatic methods have been developed among which boundary and region based approaches constitute two major categories.

Snakes, initially introduced by Kass and Terzopoulos [1], are the primary groups of boundary based methods. Various alternatives for reducing dependency of these methods on initialization are proposed, e.g., a constant evolving force by Cohen [2] and an adaptive force by Xu and Prince [3]–[4] known as Gradient Vector Flow (GVF). To increase the robustness of these models, orthogonal gradient components are considered [5]. However, numerical errors are inevitable problems in estimating important geometric parameters such as normal vector and curvature.

The level set method is developed as an implicit representation of contours to overcome the numerical errors in addition to simplicity of extending to higher dimensions. It follows topological changes and extracts accurate geometric parameters such as curvature $k=\nabla \cdot \vec{n}=\nabla \cdot \frac{\nabla \varphi}{|\nabla \varphi|}$ (where $\varphi$ is almost always the signed distance function in which $|\nabla \varphi| =1$) [6]. In the level set method, an appropriate embedding function $\varphi: I \times [0\ T] \rightarrow R$ is used to implicitly propagate boundaries $C(t)$ in the image plane ($C(t) = \{x \in I| \varphi(x, t) = 0\}$) [7]–[8]. The level set theory is used to find a solution to the evolution equation. To this end, solving the Euler equation ( $\frac{\partial \varphi}{\partial t}=F|\nabla \varphi|$) for $\varphi$ and finding pixels in which $\varphi$ equals zero yields the boundary, where $\varphi$ is the level set function and $F$ is the evolving force [4],[9]. Efficient numerical methods are proposed for solving this equation, such as fast marching and narrow band methods [10]–[11]. Various boundary based models are proposed based on the advantages of the level set method. In classical methods, the following equation is used.

$\frac{\partial \varphi}{\partial t}=c(x)(\kappa+V_0)|\nabla \varphi|+(\nabla c+\nabla \varphi)+\frac{V_0}{2}(x \cdot \nabla c)|\nabla \varphi|$ where $V_0$ (constant force) and $\nabla c. \nabla \varphi$ (advection term) help with the detection of weak boundaries [12]. In the geodesic active contours, the evolution equation $\frac{\partial \varphi}{\partial t}=g(I)(\kappa+c)|\nabla \varphi|+\nabla g(I) \cdot \nabla \varphi$ is used where $g(I)=\frac{1}{1+|\nabla[G_\sigma * I(x)]|^p}$ is the evolving force and $p$ is either 1 or 2. Here, $c$ serves as a constant velocity and helps with the extraction of weak boundaries [8].

Prior work on boundary based methods and their related flaws are numerous. For solving their problems, region based methods are introduced. These methods are related to statistical methods, texture based approaches, and clustering. Active contours without edges and density based methods are also considered in this group. Intensity histogram (parametric or non-parametric) and the variance of the image intensities are examples of the quantities used in the region based methods [13]–[14]. Statistical methods may also use intensity information [15] or curvature gradients in addition to shape index for each pixel or voxel [16]–[17]. The probabilities of each pixel belonging to each class are estimated using the label parameters and the prior probabilities. Then, each pixel is associated with the class that has the maximum posterior probability. Mixture models are also commonly used in the statistical segmentation methods. Recent work provides inference on fully adaptive spatial mixture models combining a variational Bayes approximation with a second-order Taylor expansion of the components of the posterior distribution [18].

Clustering methods form a group of region based approaches that use most discriminating features extracted from the image regions. By associating each feature vector to only one class or to all classes with deferent levels of association, crisp or fuzzy clustering methods are derived, where fuzzy clustering methods are widely used in image segmentation [19]. The key point here is that although fuzzy methods are appropriate for segmenting tissues, but segmenting structures requires additional complementary methods. Using the distance between two pixels based on a homogeneity criterion and an object similarity measure as the fuzzy characteristics, fuzzy-connected methods are developed for image segmentation.

Computational complexity of these methods is their main weakness for segmenting brain structures when compared with other methods [20]. In their application to brain structure segmentation, the Sulcal Findi is segmented by finding connected regions exceeding a depth threshold based on a geometric depth measure [21]. Moreover, there are methods that combine the boundary and region information [22]–[23].

Active contours without edges are also considered as another group of region based methods that are based on Mumford-Shah method. Minimizing specific energy term which results in two separate regions with most homogeneity [24] makes these methods proper for segmenting structures that have weak boundaries. In addition, structures whose inside intensity are either higher or lower than their outside can be segmented by such methods. This partitioning criterion, however, may fall into trouble when segmenting structures such as thalamus with sides reaching cerebrospinal fluid (CSF) with high contrast and sharp edges and other sides being adjacent to white matter with low contrast and weak edges [25]–[26].

Texture based methods are applicable to images with specific patterns and high signal-to-noise ratio (SNR). The ways the textons, as texture elements, are defined result in different texture based approaches. Updating the probability density function (pdf) of each pixel and comparing it with the one belonging to textons, regions with specific textons may be segmented [27]. Genetic algorithms are used as an alternative method for finding the optimal texton and segmenting desired regions of the image [28].

In other attempts, shape models are developed using Principle Component Analysis (PCA) which uses the signed distance function from the average [29]–[30]. PCA may be used to evaluate the distribution function of shape parameter based on the training samples [30]. This method is limited to the parametric deformation between the reference shape and the evolving contour [31]–[32]. Also, covariant shape deformations of neighboring structures may be used as another source of a priori information [33]. Likewise, there are methods that use a shape prior as a functional of the distance between the evolving contour and the reference curve [34]–[35]. Although the use of shape models may increase the segmentation accuracy, it requires statistical information about the shape of the structure [36].

Exploring the literatures, it is noted that all available medical information is not used in the segmentation process. None of the existing methods is suitable for structures that have both weak and strong boundaries. In addition, when the structures of interest in the testing datasets are different from the training datasets in terms of their shapes or locations, these methods generate inaccurate segmentation results. In this paper, we present on a promising method that is based on general anatomical constraints consistently found in different subjects. This is in-line with recent efforts by other groups in applying anatomical constraints such as those defined based on fuzzy spatial relationships [37] and selection of the lateral ventricles as anatomical landmarks for the segmentation of the caudate nucleus [38]. It is also inline with the methods that use spatial information from an atlas besides the likelihood functions estimated from the training datasets, e.g., Akselrod-Ballin et al [39].

Our proposed method is based on three novel ideas: 1) estimation of the entropy dynamically for multiple structures; 2) inclusion of a symmetry criterion based on the general symmetry of the brain structures in the two hemispheres; and 3) addition of a force based on the tissue type information to keep the contours in the correct tissue type.

The main idea of the proposed method is to replace complex energy terms by anatomical knowledge that improves segmentation of specific structures. In addition, inclusion of structures that are from the same tissue type in the pdf estimation process improves the estimation results. Consequently, the segmented structures are most homogenous and accurate [40]–[41] and capable of preserving more details of the structures. Furthermore, by including

a novel constraint based on the fact that the structures are symmetric in general, the segmentation results become almost independent of initialization unlike many other methods proposed in the past. Last but not least, using fuzzy c-means clustering, structures shape information is used in the segmentation process, making the proposed method independent of the statistical information unlike the statistical methods discussed above [29]–[31]. All together, these three novel forces can segment the brain structures accurately even if the evolving curves are improperly initialized. The details of the structures are preserved mainly due to the dynamic entropy estimation and the fuzzy clustering method applied in this method.

The proposed method segments double-sided structures (existing in both hemispheres) accurately. The results of using multi-structural pdf's in the segmentation of caudate and ventricle are compared with those of the single structure. In addition, using a fuzzy tissue type criterion, the caudate is segmented accurately even when the initial contour is inappropriate (covers both of the caudate and ventricles). This shows robustness of the proposed method to the accuracy of the initialization process. It should be noted that although the symmetry force may not play a positive role when there are structural deformations in the brain, the method may still preserve robustness based on the other two forces (dynamic entropy optimization and fuzzy tissue type criterion). For example, asymmetric ventricles segmented and shown in this paper serve as an illustration of this property. However, if there are large deformations in the brain, the proposed method may be incapable of segmenting the structures. This also holds for other state-of-the-art methods and is attributed to the large deformations of the brain structures that are not considered in the a priori knowledge (shape models) used in the current automatic segmentation methods.

The rest of the paper is organized as follows. The proposed method is explained in Section II. Experimental results are presented in Section III and conclusions are given in Section IV.

## II. Proposed Method

The proposed method is most appropriate for the segmentation of structures that are of the same tissue type, e.g., gray matter, like putamen and caudate and are also similar on both sides of the brain. The constraint that the related structures are composed of the same tissue type increases the accuracy and reduces dependency of the segmentation results on the model parameters and the initialization process. Based on the anatomical texts such as [42], certain brain structures like putamen and caudate are composed of the same tissue type and have very similar shapes in the two hemispheres. Therefore, it is beneficial to minimize a density-based energy of the structures that are made of the same type of tissue. Also, a symmetry force should improve the segmentation results. The benefit of using the symmetry interaction is shown by improperly initializing the contour. Without using the symmetry interaction, the algorithm is much more parameter dependent.

Almost all of the current methods depend on the initial contour unless this dependency is reduced by using the training datasets and approximating the locations and the shapes of the desired structures. This makes such methods dependent on the selected datasets and the registration process. To avoid this dependency, an energy term is used that minimizes misplacement of the model on the desired tissue. In our method, each image is clustered into 5 tissue classes: 1) background; 2) skull; 3) CSF; 4) gray matter; and 5) white matter. Using the proposed criterion, improper initial contours are moved to the desired tissue. For instance, since ventricles and caudate are from different classes, when the initial contours overlap both tissue classes, this moves the caudate model away from CSF.

### A. Dynamic Density Based Energy Optimization

Image segmentation can be viewed as a function optimization process. In this view, entropy is an appropriate objective function for optimization due to its close relationship with the image intensity uniformity in the segmented region. In the proposed method, the entropies of multiple evolving contours are minimized simultaneously to find regions with most uniform intensities. To estimate the entropy, the pdf's of the structures are needed. Since there are multiple structures in the brain that are made of the same tissue type, all of these structures are used in the estimation process to increase its accuracy. Note that this estimation is done in each iteration of the algorithm and thus it is called "dynamic" in this paper. Then, to solve the evolution equation, the level set theory is applied. In this method, the active contour is equal to the zero crossing of a higher dimensional signed distance function $\varphi(x, t)$. Using $\varphi: I \times [0\ T] \rightarrow R$ as the embedding function, it is possible to implicitly propagate boundaries $C(t)$ in the image plane such that $C(t) = \{x \in I | \varphi(x, t) = 0\}$ [10].

Suppose that the evolving contour is represented with $C(t)$: $[0, \infty] \rightarrow R^N$ and the initial contour is identified by $C(0)$. $\varphi(x, t = 0)$: $x \in R^N$ is introduced so that $\varphi(x, t = 0) = \pm d$ is the distance between the point $x$ and the initial contour $C(0)$. The final boundary is generated by solving the Euler equation of $\varphi$ and finding pixels in which $\varphi$ equals zero [12], [43]. The evolution equation can be written as:

$$\frac{\partial \varphi}{\partial t} = F|\nabla \varphi| \tag{1}$$

where $\varphi$ is the level set function and $F$ is the evolving force that pushes the contour towards the desired boundaries.

The proposed method optimizes a functional based on the information theory. The first term of this functional is named $\phi(q(I(x), \Omega))$ and is based on the work of Herbulot, et al [40] and Jehan-Besson, et al [44]. It can be considered as a homogeneity descriptor since it describes the complexity of a region. Therefore, the final contour will surround a region with maximum homogeneity or minimum entropy. This term is defined as:

$$\phi(q(I(x), \Omega)) = -q(I(x), \Omega)\ln(q(I(x), \Omega)) = E_{ent}(x) \tag{2}$$

where $q(I(x), \Omega)$ is defined in Eq. (3) and is an estimate of the pdf of the intensity values in the region surrounded by the contour. For maximal robustness, the estimation is done using the region $\Omega$ which includes regions of all of the desired structures that are from the same tissue type. The Parzen window method is applied to estimate $q(I(x), \Omega)$ as:

$$q(I(x), \Omega) = \frac{1}{|\Omega|}\int_{\Omega} K(I(x) - \widehat{I(x)})d\widehat{x} \tag{3}$$

where $K$ represents the Gaussian kernels with the zero mean and standard deviation of $\sigma$.

As shown in Figure 1, the pdf $q(I(x), \Omega)$ is estimated using pixel intensities inside both of the green and red contours since they are all composed of gray matter. For the ventricle system, $\Omega$ consists of the ventricles on both hemispheres that include CSF.

Using the shape gradient method and a dynamic scheme, the objective function can be written as:

$$J(\Omega(\tau))=\int_{\Omega(\tau)}(\phi(q(I(x),\Omega(\tau)))dx \tag{4}$$

where the region $\Omega(\tau)$ depends on an evolution parameter $\tau$ and consists of all models with the same tissue type. The $\Omega(\tau)$ changes in each iteration based on the curve evolution and results in a new region with a new pdf and therefore a different entropy. The new pdf is estimated using Eq. (3) but $\Omega$ is updated in each iteration. This means that a dynamic version of Eq. (2), i.e., $q(I(x),\Omega(\tau))=\frac{1}{|\Omega(\tau)|}\int_{\Omega(\tau)}K(I(x)-\widehat{I(x)})d\widehat{x}$ is used to estimate the pdf in each iteration of the algorithm.

To establish the curve evolution equation, $J(\Omega(\tau))$ is differentiated with respect to $\tau$ to yield:

$$\begin{aligned}dJ_r(\Omega,V)=&\int_{\Omega}\phi'_r(q(I(x),\Omega),V)dx\\&-\int_{\partial\Omega}\phi(q(I(s),\Omega)(V\cdot N)ds\end{aligned} \tag{5}$$

where $N$ is the unit inward normal of the contour and $\phi'_r(q(I(x),\Omega),V)$ represents the derivative of $\phi$ in the direction of $V$. Computing the domain derivative $\phi'_r$ [40],[44]–[45], the following equation is obtained for the evolution of the contour:

$$\begin{aligned}F_{entropy}=\frac{\partial\Gamma}{\partial t}=[&-q(I(\widehat{x},\Omega))(\ln q(i(\widehat{x},\Omega))+1)-\frac{1}{|\Omega|}(E(\Omega)-1\\&+\int_{\Omega}K(I(x)-I(\widehat{x}))\ln q(I(x),\Omega)dx]N\end{aligned} \tag{6}$$

Using the results, a region-based objective function is defined as [44]:

$$J(\Omega_{in},\Omega_{out})=E^{\Omega_{in}}_{entropy}+E^{\Omega_{out}}_{entropy}=E^{\Omega}_{entropy} \tag{7}$$

in which there is a competition between the background and object regions.

### B. Fuzzy Tissue Type Force

Dependency of the segmentation results on the initial contour may be reduced by using the training datasets to model the shapes and locations of specific structures. However, this approach requires image registration and makes such methods dependent on these datasets. To avoid these limitations, we apply the fuzzy c-means clustering algorithm on each image individually to segment white matter, gray matter, and CSF. This allows integration of the tissue type information (prior knowledge) into the segmentation process and makes the proposed segmentation method independent of the statistical information required in the statistical methods.

Using a set of functions $u_j: X\rightarrow A, j = 1,..,m$ with $A = [0, 1]$, the vector $X$ belongs to all clusters. The following cost function is most commonly used in fuzzy clustering [19].

$$J_q(\theta, U)=\sum_{i=1}^{N}\sum_{j=1}^{m}u_{ij}^{q}d(x_i,\theta_j) \tag{8}$$

where $d(x_i, \theta_j)$ can be any distance (dissimilarity) measure between the data point $x_i$ and the $j$-th cluster center ($\theta_j$) and $q$ is the fuzziness coefficient. Minimizing $J$ with respect to $\theta$ and $U$ subject to the following constraints, the membership of $x_i$ to the $j$-th cluster is found.

$$\sum_{j=1}^{m}u_{ij}=1, \quad i=1,\ldots..,N \tag{9}$$

where

$$\begin{aligned} u_{ij}\in[0.1],\ \ i=1,\ldots,N,\ \ j=1,\ldots..,m,\\ 0<\sum_{i=1}^{N}u_{ij}<N, \quad j=1,2,\ldots,m \end{aligned} \tag{10}$$

As discussed above, by applying the fuzzy c-means clustering, each image is segmented into 5 clusters (tissue classes). In Figure 2, three main clusters (white matter, gray matter, and CSF) are shown.

Adjacency of structures like caudate and ventricles may complicate the segmentation process, especially when the initial contours cover both structures. For example, the green contours in Figure 1 that are supposed to segment the caudate may evolve incorrectly towards the blue contours that are supposed to segment the ventricles. Using the following fuzzy criterion, however, the contours gradually enter their related tissue even they are misplaced in the initialization process (this is shown later in the Results Section).

The proposed fuzzy criterion is added to the evolution equation as a second energy term. To this end, the fuzzy tissue type term is defined for the $j$-th structure as:

$$E_{fuzz_j}=\int_{\Omega_j}(H(\varphi_j(x))-fuzz_j(x))^2dx \tag{11}$$

where $\varphi_j$ is a signed distance function related to the $j$-th structure in each side of the brain and $H$ represents the step function. The $fuzz_j\,(x)$ is a function which uses the clustering results to identify the tissue related to the $j$-th structure. For instance, if the $j$-th structure is the left caudate, $fuzz_j\,(x)$ equals zero if $x$ belongs to gray matter (GM) and equals one if it belongs to the other clusters.

$$fuzz_j(x)=\begin{cases} 0 & x\in GM \\ 1 & x\notin GM \end{cases} \tag{12}$$

The Euler-Lagrange equation for updating $\varphi_j$ is [44]:

$$F_{fuzz_j}=\frac{\partial \varphi_j}{\partial t}=2(H(\varphi_j)-fuzz_j)\delta(\varphi_j) \tag{13}$$

where $\delta(\varphi_j)$represents the Dirac delta function and $fuzz_j$ is the fixed function used for $E_{fuzz_j}$ minimization.

We reduce the dependency of the proposed method on the clustering results by applying fuzzy tissue type to one side of the brain (e.g., the right side) in an iteration of the algorithm. The other proposed constraint, based on symmetry is applied to the structures on the other side (in this example, left side). Consequently, combining density-based force and fuzzy tissue type, the following formula describes the total evolving force applied to the *j*-th model related to the right side structures (λ is a parameter that adjusts the impact of the fuzzy force).

$$F_j=F_{entropy_j}+\lambda \cdot F_{fuzz_j} \tag{14}$$

Note that in using $F_{fuzz_j}$, there is no need for image registration. In the next iteration, symmetry and fuzzy tissue type forces are exchanged between the two hemispheres so that application of the method is not restricted to fully symmetric brains and the clustering results (see Figure 3).

## C. Symmetry Interaction

A symmetry surface may be defined for the brain such that the structures in the two hemispheres are approximately symmetric with respect to it. This surface may be used to improve segmentation accuracy and robustness for these structures. Here, we explain our approach for defining this surface and using it in the segmentation process. The proposed dynamic curve evolution starts from two separate contours of the two structures (ventricles and caudate) in the each side of the brain. The symmetry surface is detected based on Liu and Collins's work [46]. Then, the contours are reflected with respect to the symmetry surface to segment the structures on the other side of the brain.

**C.1. Symmetry Surface Definition—**There are several methods for the defining the symmetry surface. Some methods maximize the correlation between the image and its reflection with respect to the symmetry surface and others optimize other similarity measures [47]. We use Liu and Collins's method [46] to find the symmetry line (axis) in each slice. Using the symmetry axes of all slices, the surface of reflection is found for the entire volume. In this method, by rotating and cross-correlating the rotated image with its vertical reflection about the center, the offsets of the symmetry axis is found; see [46] for details.

**C.2. Symmetry Interaction—**As mentioned previously, in an iteration of the algorithm, the symmetry constraint is added to the evolution of the contour on one of the hemispheres (e.g., left side). To this end, the shape symmetry term is defined for the *j*-th structure as:

$$E_{sym_j}=\int_{\Omega_j^s}(H(\varphi_j^L)-H(\varphi_j^R))^2 dx \tag{15}$$

where $\varphi_j^L$ and $\varphi_j^R$ are signed distance functions for the *j*-th structure in the right and left hemispheres, respectively. The Euler-Lagrange equation for updating $\varphi_j^L$ is [44]:

$$F^L_{sym_j}=\frac{\partial \varphi^L_j}{\partial t}=2(H(\varphi^L_j)-H(\varphi^R_j))\delta(\varphi^L_j) \tag{16}$$

where $\varphi^R_j$ is chosen to be a fixed sign distance function for $E^L_j$ minimization.

Combining the symmetry force and the multi-structural density-based criterion, the following formula describes the total evolving force applied to the *j*-th left side model (λ is a parameter that adjusts the impact of the symmetry force).

$$F^L_j=\lambda \cdot F^L_{sym_j}+F^L_{entropy_j} \tag{17}$$

Note that using the symmetry interaction reduces dependency of the proposed method on the fuzzy clustering results, represented by the fuzzy tissue type force. It increases the robustness of the method by integrating anatomical information in the segmentation process.

### D. MRI Datasets

The MRI datasets used in this work and their manual segmentations are obtained from the Center for Morphometric Analysis at Massachusetts General Hospital, available at IBSR [48]. For each subject, T1-wighted volumetric images with slightly different voxel sizes ($0.938\times0.938\times1.5$ mm$^3$, $1.0\times1.0\times1.5$ mm$^3$, $0.837\times0.837\times1.5$ mm$^3$) are used but normalized to the Talairach orientation (rotation only). The images are processed by the CMA "autoseg" bias field correction routines to remove the field inhomogeneity effects from the images. The 3D-Slicer software [49] was used for visualization of the results.

### E. Summary of Proposed Method

For a step-by-step presentation of the proposed method, a flowchart of the steps of the method is provided in Figure 4 and described below.

As discussed in the above subsections, the proposed method is based on dynamic entropy estimation, fuzzy tissue type criterion, and symmetry interaction. Initialization is done manually for one hemisphere while it is done automatically for the other by estimating the symmetry plane of the brain and reflecting the initial contours to the other hemisphere. Next, in each iteration of the algorithm, the aforementioned forces are calculated and applied on each evolving contour. To minimize the chances of incorrect evolutions of the models, in each iteration of the algorithm, one of the symmetry or fuzzy tissue type forces is applied to one of the hemispheres and the other to the other hemisphere. This is switched between the hemispheres in the next iteration to allow the method to work properly even when the two hemispheres are not fully symmetric. The steps of the proposed method, also shown in Figure 4, are as follows.

1. Manual initialization on one side (e.g., right side).
2. Detection of the symmetry plane, reflection of the initial contours, and initialization on the other side.
3. Calculation of the following three criteria:
    3.1. Dynamic entropy minimization over the regions with the same tissue type.
    3.2. Fuzzy tissue type force based on the fuzzy c-means clustering method.

3.3. Symmetric criterion that tries to evolve the contours similar to the other side.

## III. Experimental Results

This section is composed of three parts. In the first part, experimental results of applying the proposed method to the segmentation of the caudate are presented. Here, impacts of the parameters and each of the proposed constraints on the segmentation results are discussed. Segmentation of the ventricles is described in the second part. Application of the proposed method to thalamus and putamen and comparison of the results of the proposed method with those of previous methods are explained in the third part. The quality of the segmented structures is evaluated using the Dice similarity and Hausdorff distance measures [50]. The Hausdorff distance is measured in the units of voxel.

Table 1 compares the accuracy of the 3D segmentation of the caudate for different values of the parameter $\lambda$ for MRI data of 6 subjects. Although $\lambda$ in (14) and (17) can be selected differently, we use the same value for both. Note that the accuracy varies slightly among the subjects but its variation is negligible. The mean value of the similarity measure changes about 1% when $\lambda$ varies in the range of 0.1 to 1. Statistical tests (pair-wise t-tests) are done to evaluate the dependency of the proposed method on $\lambda$. The average and standard deviation of the resulting p-values are $0.44\pm0.31$, indicating that there is no significant difference between the results obtained for different values of the parameter $\lambda$. The segmented caudates are shown three-dimensionally in Figure 5. They are shown slice by slice in Figure 6. In all experiments, the initial contours are placed on the desired structures similar to what is done using a brain atlas.

The proposed fuzzy tissue type, symmetry interaction, and estimation of pdf's using all structures of the same tissue type have increased robustness of the segmentation method and decreased its dependency on the initial contours. To illustrate this, Figure 7 compares the segmentation results of using various initializations. Improper initializations use contours that overlap two neighboring structures or tissue types (e.g., white matter and gray matter or gray matter and CSF). This figure shows that the proposed approach guides the improper initialization towards correct segmentation without a need to change the model parameters. Table 1 illustrates that the results of the proposed method are independent of the initialization and the parameter $\lambda$. Table 2 lists accuracy of the extracted caudate on each of the selected slices shown in Figure 6 evaluated using the Dice measure, confirming accuracy of the results. Pair-wise t-tests are done to evaluate dependency of the performance of the method on the variations in different slices through the structure. The p-values of the t-tests for the first and second, first and third, and second and third slices are 0.66, 0.02, and 0.01, respectively. These results indicate that the performance of the method on the third slice is different from those of the other slices. This is also visible in the summary statistics in the last row of Table 2.

We have compared our proposed method with two strong region based methods: active contour without edge [25]; and Herbulot's density based optimization [40] in Figure 8. The active contour without edge method is a strong region based method. However, since the gradient information is ignored in this method, it is not capable of accurately segmenting structures like caudate that have both weak and strong edges; see Figure 8(a). In Figure 8(b), the segmented caudate is shown using the Herbulot's method. This method does not segment the caudate correctly unless the initialization and model parameters are selected properly. However, using the same initialization and parameters, the results improve when dynamic density based minimization is applied; see Figure 8(c). In Figures 8(d)–(e), the effects of including symmetry and fuzzy tissue type are shown. The caudate segmented using all of the proposed steps with $\lambda = 0.6$ is shown in Figure 9(f). Table 3 shows the effect of using each of the constraints in the

segmentation of the caudate by the Herbulot's density based method. As shown, each of the proposed constraints increases the segmentation accuracy when the same initialization is used.

Table 4 shows accuracy of the segmentation of the ventricles by the proposed method for different values of the parameter $\lambda$ using MRI of eight subjects. Note that the method is robust with respect to the subjects and parameter changes. As shown in the last row of the table, the mean value of the similarity measure changes only about 1% when $\lambda$ varies in the range of 0.1 to 1. Pair-wise t-tests find the average and standard deviation of the p-value to be $0.41\pm0.25$, confirming independency of the results from the parameter $\lambda$. The final segmentation results of the ventricles for 6 of the subjects are shown in Figure 9.

We have noticed that with appropriate initialization, Herbulot's density based method works fine in segmenting high contrast structures such as ventricles that are surrounded by regions with higher or lower intensity on all sides. However, with improper initialization, this method does not work properly and the proposed constraints improve the results. Figure 10 shows this problem and the effect of dynamic pdf estimation, symmetry interaction, and fuzzy tissue type on the results. Figure 10(a) shows the ventricles segmented using the Herbulot's method. Note that the ventricles are not segmented correctly. Using the same initialization and model parameters, the segmentation results are improved as the proposed steps are applied; the results are illustrated in Figures 10(b)–(e). These improvements are quantified in Table 5.

To evaluate the effect of the proposed multi-structure pdf estimation method, a comparison is presented for the single structure (model) versus multi-structure (multi-model) estimation when using an improper initialization. Figure 11(a) shows the results when each model evolves using its own information (pdf is estimated using the region defined by the model). Figure 11 (b) show the results when all four models are used in estimating the pdf. Note the improvement achieved by using multiple regions for the estimation of the pdf.

Finally, to compare the proposed 3D method with our previous 2D methods, we have segmented putamen, ventricle, caudate, and thalamus in 2D. Table 6 quantitatively compares the segmentation results of 4 brain structures in 8 subjects, illustrating applicability of the proposed method for their segmentation. Comparing the summary statistics on the last row of the table with those of the Tables 1 and 4 shows that the performance of the 2D method for different subjects is more variable than that of the 3D method. Table 7 compares the results of the proposed method with those of three previous methods. The first method is a combination of gradient and active contour without edge methods [22]. This method is developed specifically for the segmentation of thalamus and structures with both weak and strong edges like caudate and thus works well for them. The second method (symmetry and statistical prior shape) uses training datasets to extract prior shape model. To extract the prior shape of each structure, a cardinality metric is used where caudate and ventricle are labeled and the registration metric counts the number of corresponding pixels that have the same labels. Amoeba method is used to optimize the metric, which does not require analytical derivatives of the metric. The ITK [51] and SPM [52] software are used for the registration of the labeled datasets and intensity volumes, respectively. This method works well for low contrast structures with weak edges like putamen and thalamus, as also shown by the results listed in Table 7. It outperforms the proposed method of this paper for these particular structures but the proposed method of this paper has the advantage of not needing any training datasets [53]. The third method uses fuzzy tissue type in addition to dynamic pdf estimation [54] and its segmentation results are quantitatively evaluated and reported in the third row of Table 7. Quantitative evaluation of the segmentation results of the proposed method are listed in the last row of Table 7. Note that the proposed method generates most accurate results for caudate and ventricles that have been its focus. Sample 3D segmentation results of the proposed method for caudate and ventricles are illustrated along with those of an expert in Figure 12.

## IV. Conclusions

This paper presents a novel, robust, multi-structure segmentation method for the segmentation of double-sided structures. To overcome two common problems in automatic segmentation of the brain structures (sensitivity to improper initialization and parameter selection), a novel method is proposed to integrate approximate symmetry of structures in the two hemispheres, tissue type of the structures, multi-structural estimation of pdf, and density based optimization. The proposed method generates homogenous structures in terms of their tissue type and is robust to improper initialization and parameter selection. Experimental results show that the proposed symmetry interaction decreases dependency of the method on initialization. The proposed use the tissue types in the image alleviates the need for prior statistical information about the structures. Robustness of the proposed method is shown by illustrating that the results it generates using proper and improper initializations are very similar. Other methods do not segment the desired structures accurately if the initialization is improper.

In the first step of the proposed method, the proposed dynamic pdf estimation improves the segmentation accuracy without a need to change initialization or models parameters. When segmenting the caudate, our use of more gray matter than the other tissues such as CSF in pdf estimation increases the probability of having more of the desired tissue (gray matter) in the segmented structures than other tissues and thus improves the segmentation accuracy.

Applying the active contour without edge as a strong region based method, it is shown that such methods are not appropriate for segmenting structures that have both weak and strong edges, e.g., caudate. They are however suitable for segmenting structures that have weak boundaries only. Comparing the proposed method with this type of region based method, superiority of the proposed method in segmenting the caudate without changing the parameters or the initialization is established. In addition, as explained previously, boundary based methods are also unable to segment structures with both types of boundaries.

In most of the previous methods, the tail of the caudate which is a challenging part of the structure is omitted. Our results, evaluated for the entire volume without cutting the tail, show that the proposed multi-structural density based optimization generates homogenous structures in terms of their tissue type. In addition, many of the previous papers lack quantitative evaluation of the segmentation results [55] and those with quantitative evaluation use a number of 2D slices for this purpose [56]. As such, we have compared the results of our proposed method on 2D slices of the volume for the caudate to those of [56]–[59], showing superiority of our method. Table 8 compares accuracy of the results of the proposed 2D and 3D segmentation methods for two brain structures with those of the corresponding methods in the literature. Note that the proposed method outperforms the others in segmenting caudate and ventricles. In addition, the tissue type information extracted from the image allows the method to work independently of the prior statistical information of the structures and the initial models.

## Acknowledgments

This work was supported in part by grants from the University of Tehran, School of Cognitive Science, Institute for Research in Fundamental Sciences, Iran Telecommunication Research Center (ITRC), and the National Institutes of Health (NIH) under grant R01-EB002450.

## References

1. Kass M. Snakes: Active Contour Models. International Journal of Computer Vision 1988;1:321–331.
2. Cohen LD. On Active Contour Models and Balloons. Graphical Model and Image Processing 1991;53:211–218.

3. Xu C, Prince JL. Snakes, Shapes, and Gradient Vector Flow. IEEE Trans on Image Processing 1998;7:359–369.
4. Xu C, Prince JL. Generalized gradient vector flow external forces for active contours. Signal Processing 1998;71:131–139.
5. Jacob M, Blu T, Unser M. Efficient energies and algorithms for parametric snakes. IEEE Trans on Image Processing 2004;13:1231–1244.
6. Malladi R, Sethian JA, Vemuri BC. Shape modeling with front propagation: A level set approach. IEEE Trans on Pattern Analysis and Machine Intelligence 1995;17:158–175.
7. Sethian, JA. Level Set Methods and Fast Marching Methods. Cambridge University Press; 2002.
8. Niessen WJ, ter Haar Romeny BM, Viergever MA. Geodesic deformable models for medical image analysis. IEEE Trans on Medical Imaging 1998;17:634–641.
9. Sapiro, G. Geometrical Partial Differential Equations and Image Analysis. Cambridge University Press; 2001.
10. Sethian, JA. Level Set Methods and Fast Marching Methods. Cambridge University Press; 2002.
11. Lefohn AE, Kniss JM, Hansen CD, Whitaker RT. A Streaming Narrow-Band Algorithm: Interactive Computation and Visualization of Level Sets. IEEE Trans on Visualization and Computer Graphics 2004;10:422–433.
12. Suri JS, Liu K, Singh S, Laxminarayan SN, Zeng X, Reden L. Shape Recovery Algorithms Using Level Sets in 2-D/3-D Medical Imagery: A State-of-the Art Review. IEEE Trans on Information Technology in Biomedicine 2002;6:8–28.
13. X. Ph.D. Thesis. University of Lausanne; Lausanne: 2005. Bresson Image Segmentation with Variational Active Contours.
14. Woolrich MW, Behrens TE. Variational Bayes inference of spatial mixture models for segmentation. Ieee Transactions on Medical Imaging 25:1380–1391. [PubMed: 17024841]
15. Rajapakse JC, Giedd JN, Rapoport J. Statistical approach to segmentation of single channel cerebral MR images. IEEE Trans on Medical Imaging 1997;16:176–186.
16. Zhang Y, Brady M, Smith S. Segmentation of brain MR images through a hidden Markov random field model and the expectation-maximization algorithm. IEEE Trans on Medical Imaging 2001;20:45–57.
17. Tu Z, Zheng S, Yuille AL, Reisse AL, Dutton RA, Lee AD, Galaburda AM, Dinov I, Thompson PM, Toga AW. Automated Extraction of the Cortical Sulci Based on Supervised Learning Approch. IEEE Trans on Medical Imaging 2007;26:541–552.
18. Woolrich MW, Behrens TE. Variational Bayes Inference of Spatial Mixture Models for Segmentation. IEEE Trans on Medical Imaging 2006;25:1380–1390.
19. Theodoridis, S.; Kourtoumbas, K. Pattern recognition. Academic Press; 1998.
20. Udupa JK, Saha PK. Fuzzy connectedness in image segmentation. Proceedings of IEEE, Emerging Medical Imaging Technology 2003;91:1649–1669.
21. Kao CY, Hofer M, Sapiro G, Stern J, Rehm K, Rottenberg DA. A Geometric Method for Automatic Extraction of Sulcal Fundi. IEEE Trans on Medical Imaging 2007;26:1168–1171.
22. Bijari, PB.; Akhoundi-Asl, AR.; Soltanian-Zadeh, H. Thalamus Segmentation in MRI Using Region and Gradient Information in Level sets. Proceedings of the 14th Iranian Conference on Elec. Eng. (ICEE'06); Tehran, Iran. May 16–18, 2006;
23. Paragios N, Deriche R. Geodesic Active Regions and Level Set Methods for Supervised Texture Segmentation. International Journal of Computer Vision 2002;46(3):223–247.
24. Tsai A, Yezzi A, Willsky AS. Curve Evolution Implementation of the Mumford Shah Functional for Image Segmentation, Denoising, Interpolation, and Magnification. IEEE Trans on Image Processing 2001;10:1278–1301.
25. Chan TF. Active Contours Without Edges. IEEE Trans on Image Processing 2001;10:266–277.
26. Zeydabadinezahad, M. M.S. Thesis. University of Tehran; Sep. 2004 Multi-resolution segmentation of MR brain images.
27. Huang, X.; Qian, Z.; Huang, R.; Metaxas, D. Deformable-Model Based Textured Object Segmentation. International Workshop on Energy Minimization Methods in Computer Vision and Pattern Recognition,; 2005. p. 119-135.

28. Delibasis K, Undrill PE. Designing Texture Filters with Genetic Algorithm: an Application to Medical Images. Signal Processing 1993;57:19–33.
29. Tsai A, Wells W, Tempany C, Grimson E, Willsky A. Mutual Information in Coupled Multi-Shape Model for Medical Image Segmentation. Medical Image Analysis 2004;8:429–445. [PubMed: 15567707]
30. Yang J, Staib LH, Duncan JS. Neighbor-Constrained Segmentation with Level Set Based 3D Deformable Models. IEEE Trans on Medical Imaging 2004;23:940–948.
31. Montillo, AA. Shape priors in medical image analysis: extensions of the level set method. University of Pennsylvania; Feb. 2002 Technical Report # MS-CIS-02-08
32. Leventon ME, Grimson WEL, Faugeras O. Statistical Shape Influence in Geodesic Active Contours. IEEE International Conference on Computer Vision and Pattern Recognition 2000;1:1316–1323.
33. Pohl KM, Fisher J, Kikinis R, Grimson WEL, Wells WM. Shape Based Segmentation of Anatomical Structures in Magnetic Resonance Images. International Conference on Computer Vision 2005;3765:489–498.
34. Hong BW, Prados E, Soatto S, Vese L. Shape Representation Based on Integral Kernels: Application to Image Matching and Segmentation. IEEE Computer Society Conference on Computer Vision and Pattern Recognition 2006;1:833–840.
35. Chan, T.; Zhu, W. Computational Applied Mathematics. UCLA; Los Angeles: 2003. Level Set Based Shape Prior Segmentation. Technical Report 03-66
36. Huang A, Nielson GM, Razdan A, Farin GE, Baluch DP, Capco DG. Thin Structure Segmentation and Visualization in Three Dimensional Biomedical Images: A Shape-Based Approach. IEEE Trans on Visualization and Computer Graphics 2006;12:93–102.
37. Colliot O, Camara O, Bloch I. Integration of Fuzzy Spatial Relations in Deformable Models-Application to Brain MRI Segmentation. The Journal of Pattern Recognition Society 2006;39:1401–1414.
38. Xia Y, Bettinger K, Shen L, Reiss AL. Automatic Segmentation of Caudate Nucleus From Human Brain MR Images. IEEE Trans on Medical Imaging 2007;26:509–517.
39. Akselrod-Ballin A, Galun M, Gomori JM, Brandt A, Basri R. Prior knowledge driven multiscale segmentation of brain MRI. MICCAI 2007;10:118–126. [PubMed: 18044560]
40. Herbulot, A.; Jehan-Besson, S.; Barlaud, M.; Aubert, G. Information theory for image segmentation using shape gradient. University of Nice; Dec. 2004 Technical report ISRN I3S/PR-2004-43-FR
41. Aubert G, Barlaud M, Faugeras O, Jehan-Besson S. Image Segmentation Using Active Contours: Calculus of Variations or Shape Gradients? SIAM Applied Mathematics 2003;63(6):2128–2154.
42. Henry, F.; Gray, RS.; Pickering Pick, T. Gray's Anathomy. Great Britain: Chancellor Press; 1985.
43. Osher S, Sethian J. Fronts Propagating with curvature dependant Algorithms based on Hamilton-Jacobi formulation. Journal of Computational Physics 1988;79:12–49.
44. Jehan-Besson S, Barlaud M, Aubert G. DREAMS: driven by an Eulerian Accurate Minimization Method for image and video segmentation. International Journal of Computer Vision 2003;53:45–70.
45. Aubert GG, Barlaud M, Faugeras O, Jehan-Besson S. Image Segmentation Using Active Contours: Calculus of Variations or Shape Gradients? The SIAM Journal on Applied Mathematics 2003;63:2128–2154.
46. Liu, Y.; Collins, RT.; Rothfus, WE. Automatic extraction of the central symmetry (mid-sagittal) plane from neuroradiology images. Carnegie Mellon Univ; Pittsburgh, PA: 1996. The Robotics Institute, Technical Report. CMU-RI-TR-96-40
47. Tuzikov AV, Colliot O, Bloch I. Brain Symmetry Plane Computation in MR Images Using Inertia Axes and Optimization. International Conference on Pattern Recognition 2002;1:516–519.
48. Center for Morphometric Analysis at Massachusetts General Hospital. http://www.cma.mgh.harvard.edu/ibsr/index.html
49. Medical Visualization and Processing Environment for Research. http://www.Slicer.org
50. Lu Y, Tan CL, Huang W, Fan L. An Approach to Word Image Matching Based on Weighted Hausdorff Distance. International Conference on Document Analysis and Recognition 2001;6:921–925.
51. National Library for Medicine Insight Segmentation and Registration Toolkit. www.itk.org

52. Welcome Trust Center for Neuro Imaging. www.fil.ion.ucl.ac.uk/spm

53. Bahmanbijari, P.; Akhondi-Asl, A.; Soltanian-Zadeh, H. Interactive Coupled Object Segmentation Using Symmetry and Distance Constraints. the Proceedings of the Third Cairo International Biomedical Engineering Conference (CIBEC'06); Cairo, Egypt. Dec. 21–24 2006;

54. Bijari, PB. M.S. Thesis. University of Tehran; Feb. 2007 Segmentation of Brain Structure from Magnetic Resonance Images Using Interactive Deformable Models.

55. Udupa JK, Saha PK. Fuzzy connectedness in image segmentation. Proceedings of IEEE, Emerging Medical Imaging Technology 2003;91:1649–1669.

56. Dawant BM, Hartmann SL, Thirion JP, Maes F, Vandermeulen D, Demaerel P. Automatic 3-D Segmentation of Internal Structures of the Head in MR Images Using a Combination of Similarity and Free-Form Transformations: Part I, Methodology and Validation on Normal Subjects. IEEE Trans on Medical Imaging 1999;18:909–916.

57. Worth AJ, Makris N, Patti R, Goodman JM, Hoge EA, Caviness VS Jr, Kennedy DN. Precise Segmentation of the Lateral Ventricles and Caudate Nucleus in MR Brain Images Using Anatomically Driven Histograms. IEEE Trans on Medical Imaging 1998;17:303–309.

58. Batmanghelich, N.; Soltanian-Zadeh, H.; Araabi, BN. Knowledge-based Segmentation Using Simultaneous Shape Priori and Histogram Information to Segment Brain Structures. IASTED SIP Conf; Honolulu, Hawaii. Aug 15–17, 2005;

59. Batmanghelich, N. MS Thesis. University of Tehran; 2005. Atlas-based deformable models for segmentation of brain structures in MRI.

60. Wu, Y.; Pohl, K.; Warfield, SK.; Cuttmann, CRG. Automated Segmentation of Cerebral Ventricular Compartments. Proc of International Society for Magnetic Resonance in Medicine, 11th Scientific Meeting, and Exhibition, Program No. 906; Ontario, Canada. July 10–16, 2003;

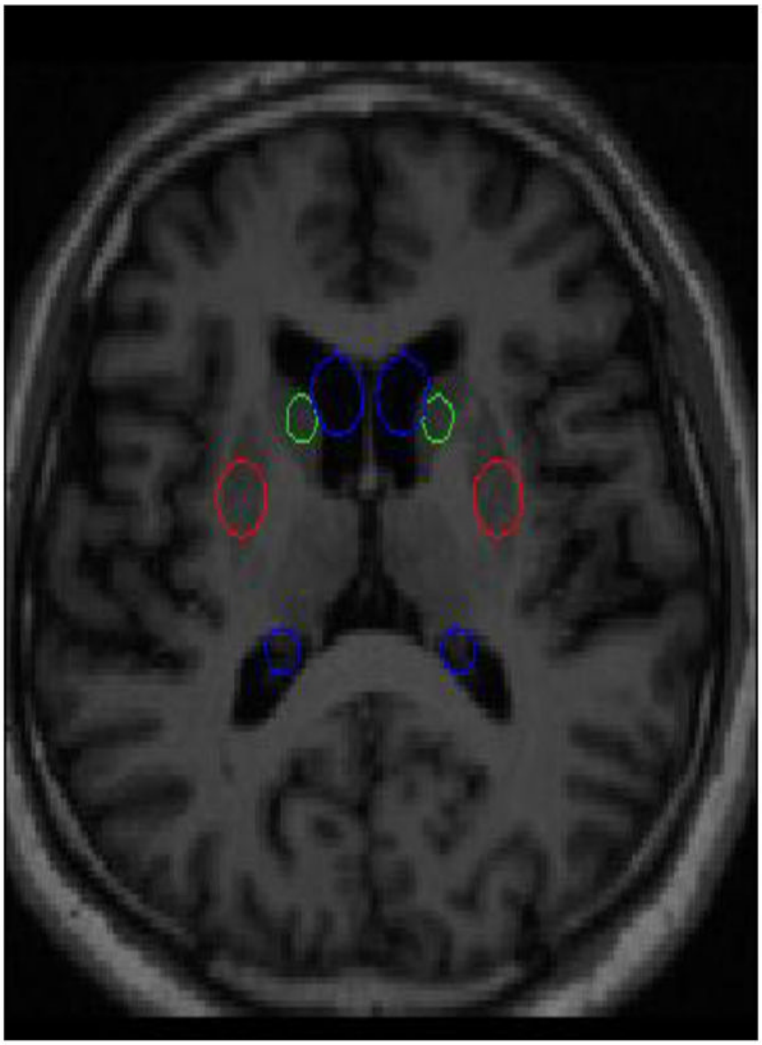

**Figure 1.**
An axial T1-weighted MR image of the brain on which initial contours for putamen (red), caudate (green), ventricles (blue) are shown.

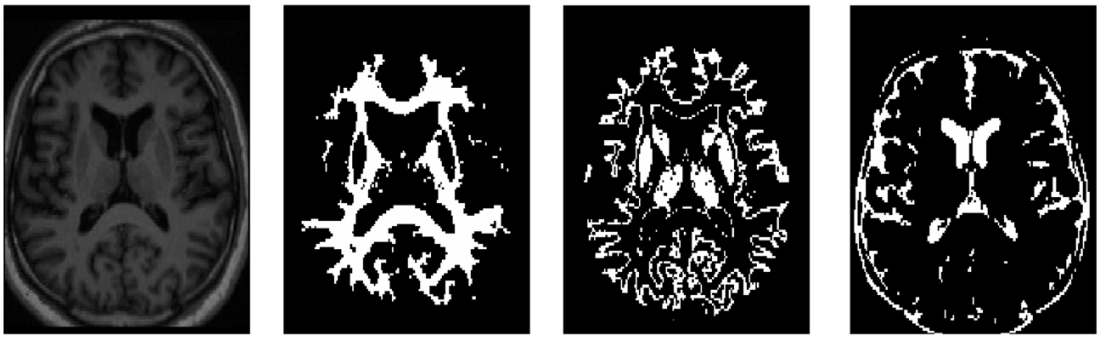


**Figure 2.**
(a) An axial T1-weighted MR image of the brain. (b) White matter cluster. (c) Gray matter cluster. (d) cerebrospinal fluid (CSF) cluster.

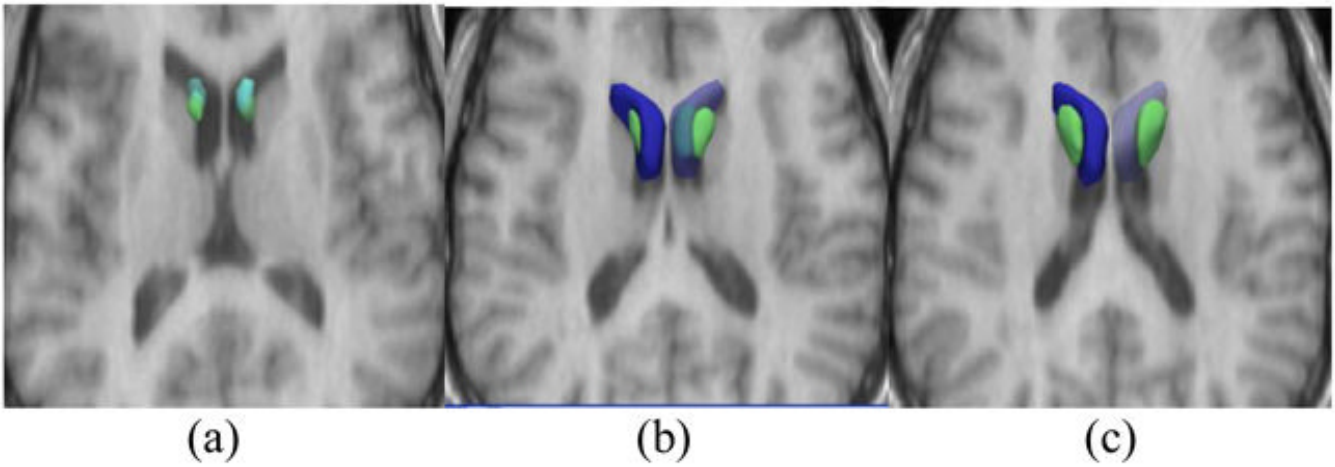


**Figure 3.**
(a) An axial T1-weighted MR image of the brain on which improper initialization for caudate and ventricles is shown. (b) The same image with the segmentation results for caudate and ventricles when no fuzzy tissue type is used. Note that the models have evolved into each other. (c) The same image with the segmentation results for caudate and ventricles when fuzzy tissue type is used. Note that here the models do not evolve into each and generate appropriate segmentation results.

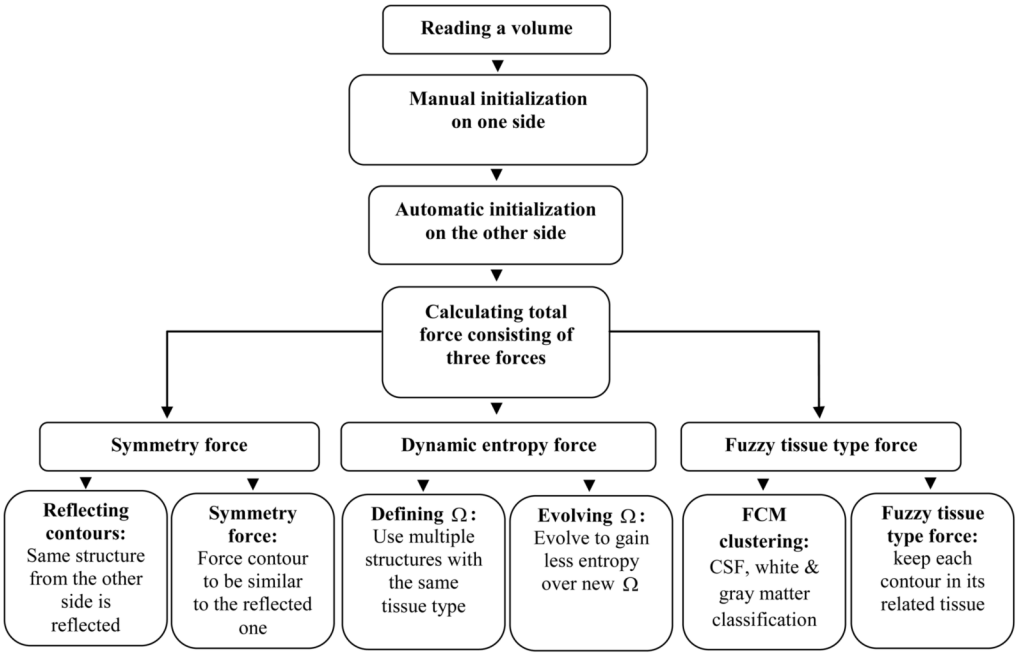


**Figure 4.**
A flowchart of the proposed method showing main steps and three forces used in the algorithm.

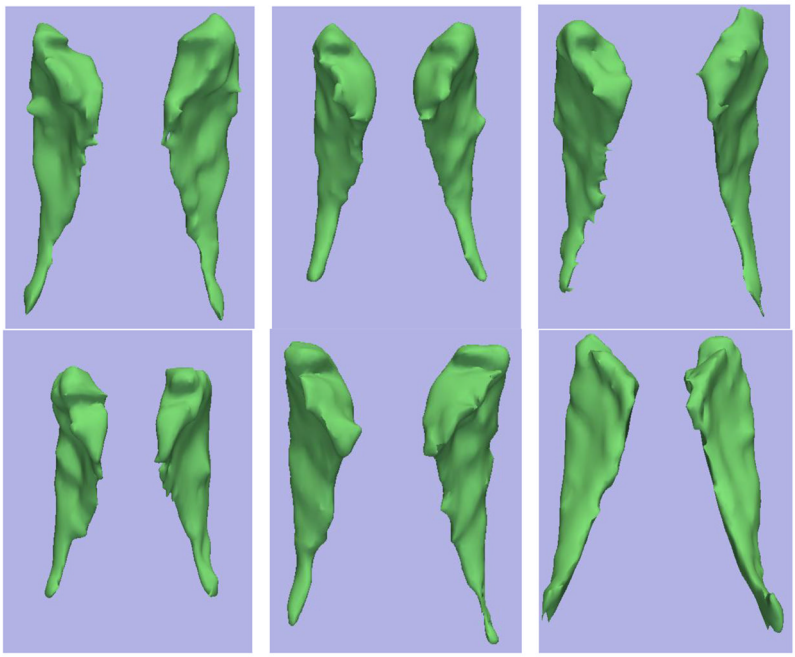

**Figure 5.**
3D visualization of the segmented caudate for 6 different subjects.

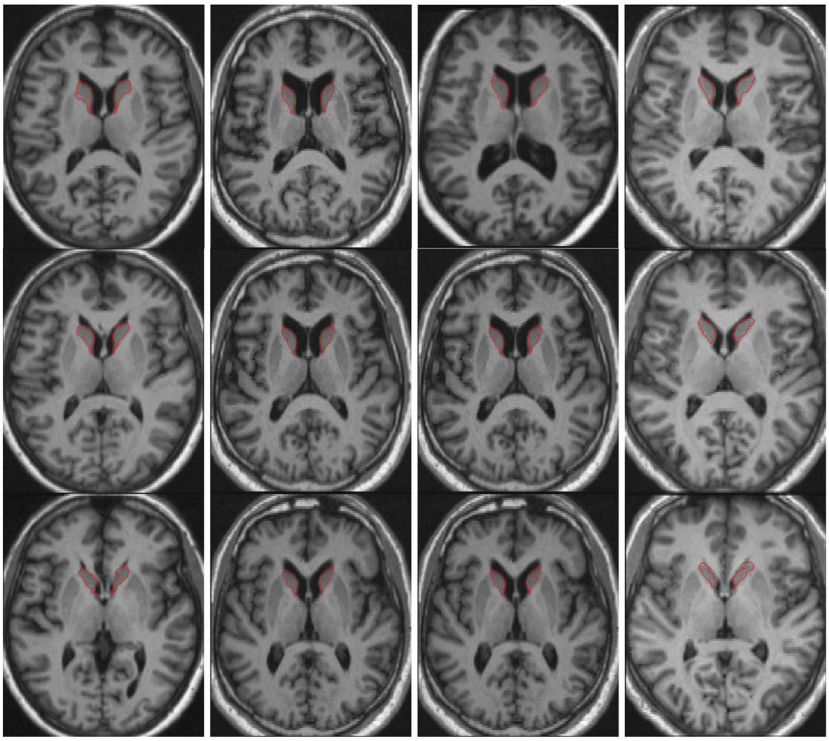


**Figure 6.**
T1-weighted MRI of 3 brain slices of 4 subjects on which and the boundaries of the segmented caudate are shown.

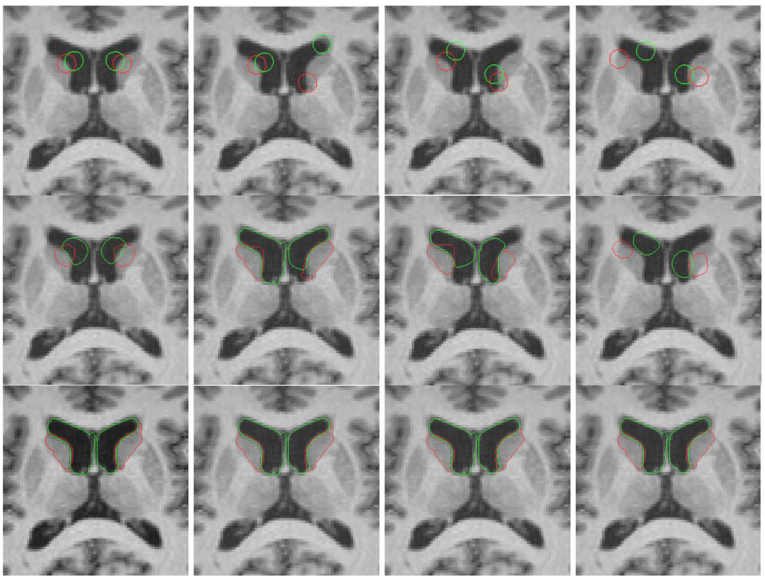


**Figure 7.**
T1-weighted MRI of a brain slice on which improper initialization and correct segmentation results are shown. First row shows the initializations. Second row shows an intermediate stage. Third row shows final segmentation of caudate and ventricles. Note that the final results are independent of the initialization.

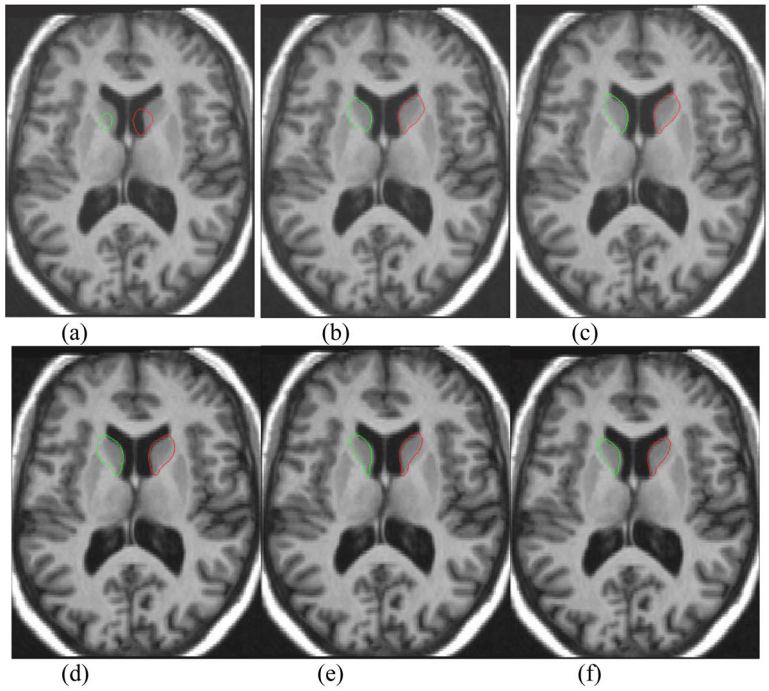


**Figure 8.**

A T1-weighted MRI on which caudate segmented by different methods are shown. (a) Active contour without edge. (b) Herbulot's method. (c) Dynamic pdf estimation is added. (d) Symmetry interaction is added. (e) Fuzzy tissue type is added. (f) Fuzzy tissue type, symmetry interaction, and dynamic pdf estimation are added with $\lambda = 0.6$.

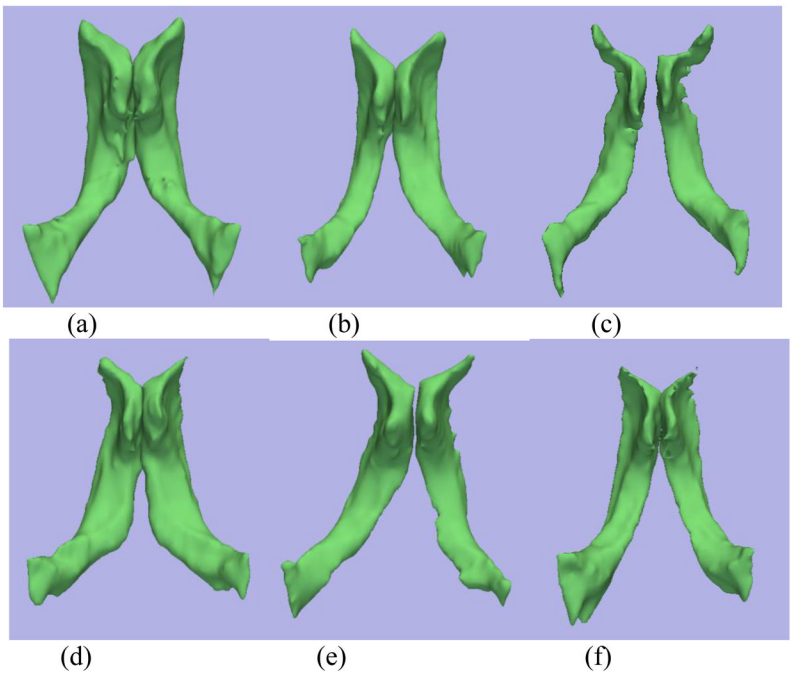


**Figure 9.**
Ventricles segmented by the proposed method for 6 different subjects.

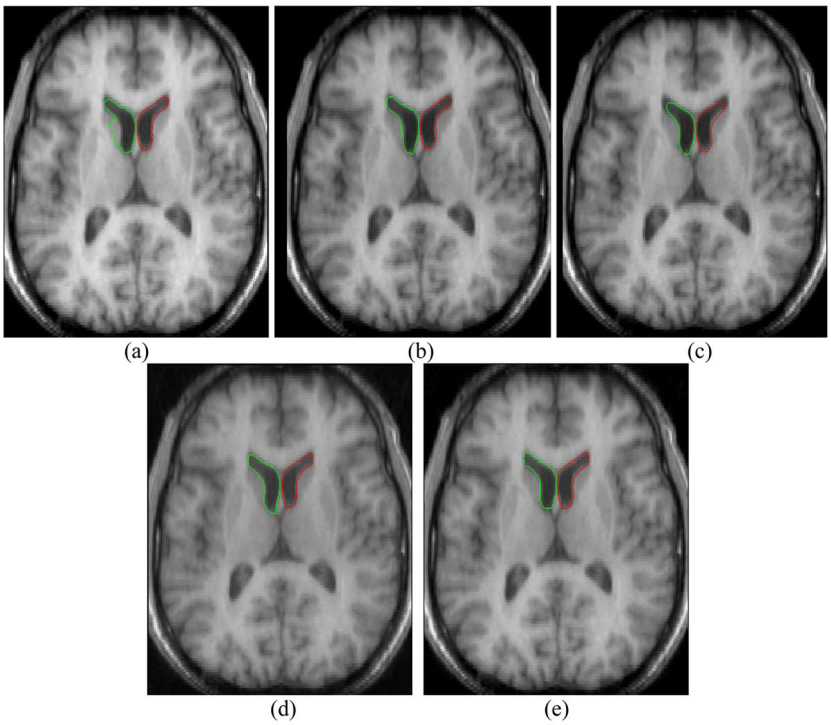


**Figure 10.**

A T1-weighted MRI on which ventricles segmented by different methods are shown. (a) Herbulot's method. (b) Dynamic pdf estimation is added. (c) Symmetry interaction is added. (d) Fuzzy tissue type is added. (e) Fuzzy tissue type, symmetry interaction, and dynamic pdf estimation are added with $\lambda = 0.6$.

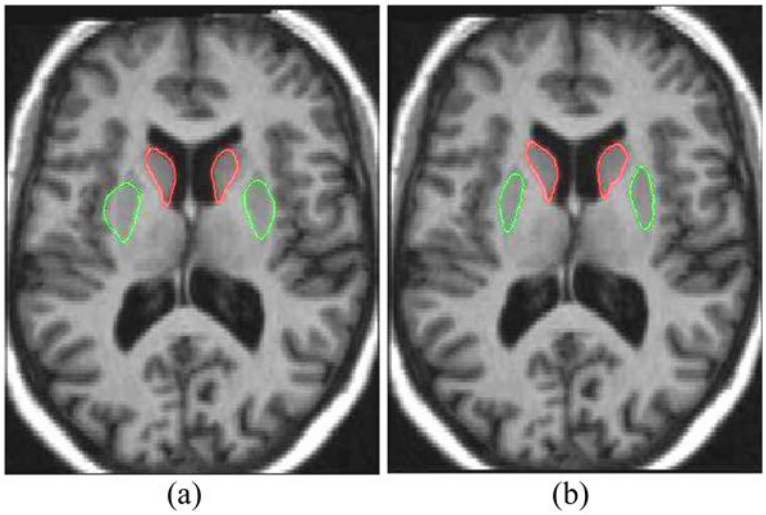


**Figure 11.**

A T1-weighted MRI on which caudate and putamen are segmented by different methods. (a) pdf is estimated using each model individually. (b) pdf is estimated using all of the models. Initializations are the same. Note the improvement in the results when pdf is estimated using all of the models.

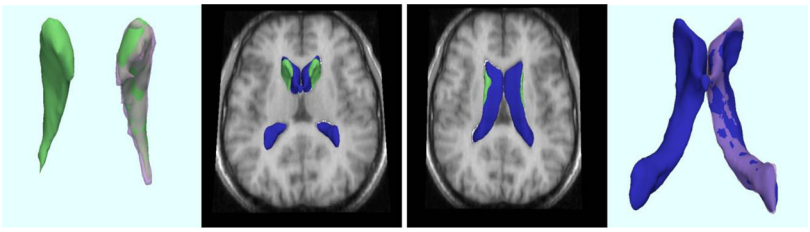

(a) (b) (c) (d)

**Figure 12.**
Final caudate and ventricle models are shown in green and blue in (a) and (d), respectively. The neurologist segmentation is shown in pepper. Final segmentation of the caudate and ventricles superimposed on 2 T1-weighted images are shown in (b) and (c).

**Table 1**

Accuracy (Dice similarity %) for 3D segmentation of the caudate as a function of $\lambda$ for 6 subjects along with their mean values and standard deviations.

| $\lambda$ | 0.1 | 0.2 | 0.4 | 0.6 | 0.8 | 1 |
|---|---|---|---|---|---|---|
| Subject 1 | 82.70 | 82.50 | 82.77 | 82.51 | 80.80 | 81.60 |
| Subject 2 | 83.00 | 82.80 | 83.06 | 82.88 | 81.18 | 82.91 |
| Subject 3 | 84.32 | 84.30 | 81.52 | 80.00 | 80.01 | 81.05 |
| Subject 4 | 80.42 | 81.54 | 81.10 | 80.01 | 80.80 | 81.10 |
| Subject 5 | 79.80 | 80.55 | 81.23 | 81.03 | 80.88 | 81.21 |
| Subject 6 | 78.14 | 78.50 | 79.11 | 79.81 | 79.01 | 80.18 |
| **mean±$\sigma$** | **81.40±2.32** | **81.70±2.01** | **81.47±1.41** | **81.04±1.36** | **80.45±0.80** | **81.34±0.90** |

**Table 2**

Accuracy (Dice similarity %) for 3 randomly selected slices of the caudate.

| Accuracy | First slice | Second slice | Third slice | Average |
|---|---|---|---|---|
| Subject 1 | 95.12 | 95.01 | 93.18 | 94.43 |
| Subject 2 | 95.15 | 95.07 | 94.05 | 94.76 |
| Subject 3 | 93.78 | 93.88 | 93.14 | 93.60 |
| Subject 4 | 94.50 | 94.50 | 92.89 | 93.96 |
| **mean±σ** | **94.64±0.65** | **94.62±0.55** | **93.32±0.51** | **94.19±0.51** |

**Table 3**

Quantitative evaluation of 2D segmentation of caudate using each of the proposed steps with the Herbulot's density based method. Accuracy and error are evaluated for both of the right and left side structures using Dice similarity % and Hausdorff distance measures, respectively.

| | **Herbulot's density based method** | **Dynamic pdf estimation added** | **Symmetry interaction added** | **Fuzzy tissue type added** | **All the steps added with $\lambda = 0.8$** | **All the steps added with $\lambda = 0.6$** |
|---|---|---|---|---|---|---|
| Error (Hausdorff distance) for the right, left sides | 4.00, 2.00 | 1.00, 1.41 | 2.00, 2.00 | 1.00, 1.41 | 1.00, 1.41 | 1.00, 1.41 |
| Accuracy (Dice similarity %) for the right, left sides | 80.18, 90.06 | 91.16, 90.26 | 90.18, 90.06 | 92.17, 91.01 | 94.11, 92.17 | 94.22, 92.47 |

**Table 4**

Accuracy (Dice similarity %) for 3D segmentation of ventricles for 8 subjects using the proposed method as a function of $\lambda$ along with their mean values and standard deviations.

| $\lambda$ | **0.1** | **0.2** | **0.4** | **0.6** | **0.8** | **1** |
|---|---|---|---|---|---|---|
| Subject 1 | 91.70 | 90.50 | 90.70 | 91.50 | 90.00 | 91.60 |
| Subject 2 | 89.70 | 90.10 | 88.80 | 89.00 | 89.10 | 90.00 |
| Subject 3 | 88.40 | 89.00 | 87.10 | 89.00 | 89.13 | 88.50 |
| Subject 4 | 92.54 | 91.55 | 91.10 | 91.71 | 90.70 | 92.15 |
| Subject 5 | 90.14 | 89.53 | 89.21 | 90.17 | 90.77 | 91.23 |
| Subject 6 | 91.20 | 90.61 | 90.67 | 91.07 | 90.87 | 91.10 |
| Subject 7 | 88.54 | 89.43 | 89.88 | 88.12 | 88.32 | 88.72 |
| Subject 8 | 88.04 | 88.25 | 89.12 | 88.87 | 87.89 | 88.15 |
| **mean±$\sigma$** | **90.03±1.67** | **89.87±1.04** | **89.57±1.31** | **89.93±1.37** | **89.60±1.16** | **90.18±1.56** |

**Table 5**

Quantitative evaluation of 2D segmentation of ventricles using each of the proposed steps with the Herbulot's density based method. Accuracy and error are evaluated for both of the right and left side structures using Dice similarity % and Hausdorff distance measures, respectively.

| Proposed forces (steps) | Herbulot's density based method | Dynamic pdf estimation added | Symmetry interaction added | Fuzzy tissue type added | All the steps added with $\lambda = 0.6$ |
|---|---|---|---|---|---|
| Error (Hausdorff distance) for the right, left sides | 1.41, 5.00 | 1.41, 1.00 | 1.41, 1.00 | 1.41, 1.41 | 1.41, 1.00 |
| Accuracy (Dice similarity %) for the right, left sides | 90.26, 80.55 | 90.26, 92.06 | 91.32, 92.06 | 91.19, 95.56 | 93.23, 95.56 |

**Table 6**

Accuracy (Dice similarity %) for 2D segmentation of 4 brain structures in 8 subjects using the proposed method. The results for the left and right hemispheres are evaluated separately.

| | Right Thalamus | Left Thalamus | Right Putamen | Left Putamen | Right Ventricle | Left Ventricle | Right Caudate | Left Caudate |
|---|---|---|---|---|---|---|---|---|
| Subject 1 | 75.41 | 68.70 | 79.41 | 90.27 | 76.92 | 82.49 | 90.27 | 90.30 |
| Subject 2 | 77.60 | 74.19 | 84.14 | 77.37 | 84.16 | 91.33 | 88.37 | 87.12 |
| Subject 3 | 68.74 | 70.21 | 65.42 | 67.17 | 82.30 | 90.55 | 91.71 | 89.57 |
| Subject 4 | 66.22 | 75.76 | 74.51 | 82.11 | 89.68 | 91.79 | 89.23 | 89.58 |
| Subject 5 | 82.00 | 78.61 | 90.58 | 87.88 | 80.90 | 87.10 | 90.20 | 91.04 |
| Subject 6 | 65.60 | 77.78 | 80.00 | 81.25 | 85.02 | 91.75 | 95.71 | 85.37 |
| Subject 7 | 80.76 | 78.41 | 87.33 | 90.41 | 85.66 | 89.67 | 90.43 | 88.65 |
| Subject 8 | 77.94 | 75.34 | 88.67 | 86.27 | 84.54 | 87.13 | 92.23 | 92.87 |
| **mean±$\sigma$** | **74.28±6.53** | **74.88±3.71** | **81.26±8.35** | **82.84±7.82** | **83.65±3.74** | **88.98±3.23** | **91.02±2.26** | **89.31±2.32** |

**Table 7**

Means and standard deviations of Dice similarity % for 4 brain structures segmented using 4 different methods in 2D.

| | Caudate (average of left and right) | Ventricles (average of left and right) | Putamen (average of left and right) | Thalamus (average of left and right) |
|---|---|---|---|---|
| Boundary and region based combination | 85.94±9.93 | 80.94±4.49 | 75.04±7.25 | 82.94±4.64 |
| Symmetry and statistical prior shape | 85.11±4.43 | 81.27±4.61 | 85.83±4.63 | 87.50±4.51 |
| Fuzzy tissue type | 89.61±2.59 | 86.11±5.09 | 77.83±9.24 | 73.11±4.71 |
| Proposed method | 90.16±2.38 | 86.31±4.35 | 82.05±7.86 | 74.58±5.14 |

**Table 8**

Comparison of the Dice similarity % (average of left and right) of the proposed 2D and 3D methods with the corresponding previous methods for the segmentation of the ventricles and caudate (-- is used to show that the value is not reported in the literature).

| 3D | Methods / Structure | Implementation of Tsai, et al [27] | Akselrod, et al [37] | ISCA [37] | Wu, et al [60] | Proposed Method |
|---|---|---|---|---|---|---|
| | Caudate | 72 | 80 | 74 | -- | 80 |
| | Ventricles | 67 | -- | -- | 83 | 90 |

| 2D | Methods / Structure | Dawant, et al [56] | Worth, et al [57] | Batmanghelich, et al [58], [59] | Proposed Method |
|---|---|---|---|---|---|
| | Caudate | 90 | 92 | 89 | 93 |